

THE MAXIMUM ISOTROPIC ENERGY OF GAMMA-RAY BURSTS

J.-L. ATTEIA¹, V. HEUSSAFF, J.-P. DEZALAY, A. KLOTZ AND D. TURPIN²

Université de Toulouse; UPS-OMP; IRAP; Toulouse, France
CNRS; IRAP; 14, avenue Edouard Belin, F-31400 Toulouse, France

A.E. TSVETKOVA AND D.D. FREDERIKS

Ioffe Institute, Politekhnikeskaya 26, St. Petersburg, 194021, Russia

Y. ZOLNIEROWSKI

LAPP, Université de Savoie, CNRS/IN2P3, 9 chemin de Bellevue, BP 110, 74941 Annecy-le-Vieux, France

F. DAIGNE AND R. MOCHKOVITCH

UPMC-CNRS, UMR7095, Institut d'Astrophysique de Paris, F-75014, Paris, France

¹jean-luc.atteia@irap.omp.eu

²D. Turpin used funds provided by the LabEx OCEVU.

ABSTRACT

The most energetic gamma-ray bursts (GRBs) are remarkable sources releasing huge amounts of energy on short timescales. Their prompt emission, which usually lasts few seconds, is so bright that it is visible across the whole observable universe. Studying these extreme events may provide clues on the nature of GRB progenitors and on the physical processes at work in relativistic jets.

In this paper, we study the bright end of the isotropic energy distribution of long GRBs. We use two samples of long GRBs with redshift detected by *Fermi*/GBM or *Konus-Wind*, two instruments which measure the spectral shape and the energetics of the prompt emission accurately. We focus on GRBs within a range of redshifts $z = 1 - 5$, a volume that contains a large number of energetic GRBs, and we propose a simple method to reconstruct the bright end of the GRB energy distribution from the observed one. We find that the GRB energy distribution cannot be described by a simple power law but requires a strong cutoff above $1 - 3 \times 10^{54}$ erg. We attribute this feature to an intrinsic limit on the energy per unit of solid angle radiated by gamma-ray bursts.

Keywords: gamma-ray bursts – cosmology – redshift

1. INTRODUCTION

Gamma-Ray Bursts are extremely energetic sources, which can release isotropic energies (E_{iso}^1) in excess of 10^{54} erg in gamma-rays. We investigate here the bright end of the GRB energy distribution with the purpose of determining whether it contains indications of a limit to the energy that GRBs radiate in gamma-rays.

The GRB energy and luminosity distributions have been the subject of numerous studies. For pre-*Swift* GRBs, these studies were based on the observed GRB redshift and peak flux distributions (Firmani et al. 2004; Guetta et al. 2005), on pseudo-redshifts (Kocevski & Liang 2006), or on theoretical considerations. The measure of hundreds of GRB redshifts with *Swift* (Gehrels et al. 2009) gave a new impulse to these studies, leading to better constraints on the shape of the luminosity and energy distributions, their evolution with redshift and the role of low luminosity GRBs (see Table 1 for a list of recent works). However, despite this strong interest for the general shape of the GRB luminosity

¹ The isotropic energy is computed under the assumption that the source emits isotropically.

function, the question of the maximum GRB luminosity or their maximum energy is rarely discussed, probably because the most energetic GRBs (with $E_{\text{iso}} \approx 10^{54}$ erg) are very rare events.

This paper discusses the existence of a limit on the isotropic energy radiated by GRBs. In Section 2, we construct the observed energy distribution of two samples of bright GRBs with well measured redshifts and spectral parameters. In Section 3, the observed energy distribution is compared with theoretical distributions with or without a cutoff at high energies, and we show that the data strongly suggest the existence of a limit to the γ -ray isotropic energy radiated by GRBs. The significance and interpretation of this limit are discussed in Section 4.

In this paper we use a flat cosmological model with $H_0 = 70 \text{ km s}^{-1} \text{ Mpc}^{-1}$ and $\Omega_M = 0.3$.

Table 1. Models of GRB luminosity function. This table summarizes how the bright end of the GRB luminosity function has been parametrized in recent works. The slope refers to the high luminosity index for broken power law models, and to the slope below the cutoff luminosity for cutoff power law models. When it is mentioned, L_{max} indicates the maximum luminosity considered in the study. δ_n is the index of the density evolution and δ_l the index of luminosity evolution described in Section 2.2.

Reference	Model	Slope	L_{br} erg s $^{-1}$	L_{cut} erg s $^{-1}$	L_{max} erg s $^{-1}$	δ_n	δ_l
Daigne et al. (2006) (SFR $_2$)	simple PL	1.6			4×10^{53}	–	–
Salvaterra & Chincarini (2007)	cutoff PL	3.5		9.5×10^{51}		–	–
	cutoff PL	2.2		0.8×10^{51}		–	1.4
Zitouni et al. (2008) (SFR $_2$)	broken PL	2.0	3×10^{51}		3×10^{53}	–	–
Dai (2009)	broken PL	1.3	5×10^{48}			–	–
Butler et al. (2010)	broken PL	3	5×10^{52}			B10 ^a	–
Wanderman & Piran (2010)	broken PL	1.4	3×10^{52}			W10 ^b	–
Salvaterra et al. (2012)	broken PL	2.3	3.8×10^{52}			1.7	–
	cutoff PL	2.1		3.1×10^{51}		1.6	–
	broken PL	1.9	0.6×10^{51}			–	2.1
	cutoff PL	2.0		0.2×10^{51}		–	2.3
Shahmoradi (2013) ^c	log-normal			2.2×10^{51}		–	–
Howell et al. (2014)	broken PL	2.6	0.8×10^{52}			W10	–
Lien et al. (2014)	broken PL	3.0	1.1×10^{52}			W10	–
Pescalli et al. (2015)	broken PL	1.8	2.8×10^{51}			–	2.5
Petrosian et al. (2015)	broken PL	3.2	1×10^{51}			–	2.3
	cutoff PL	0.5		1.4×10^{51}		–	2.3
Tan & Wang (2015) (RGRB2)	broken PL	2.4	3.9×10^{51}			W10	–
	broken PL	2.1	1.4×10^{51}			W10	0.8
Deng et al. (2016)	broken PL	2.5	1.7×10^{51}			–	1.14

^aButler et al. (2010) propose a parametrization of the GRB formation rate which cannot be represented by a simple index δ_n . We note B10 this parametrization, which predicts an excess of GRBs over the SFR of Hopkins & Beacom (2006), by a factor ~ 3.7 at redshift $z=5$.

^bWanderman & Piran (2010) propose a parametrization of the GRB formation rate, which cannot be represented by a simple index δ_n . We note W10 this parametrization, which predicts an excess of GRBs over the SFR of Hopkins & Beacom (2006), by a factor ~ 3.4 at redshift $z=5$. Various other studies use this parametrization.

^c L_{cut} gives the center of the log-normal distribution, the width of the distribution is: $\log(\sigma_L) = -0.22$.

2. THE GRB ISOTROPIC ENERGY DISTRIBUTION

2.1. Construction of two GRB samples

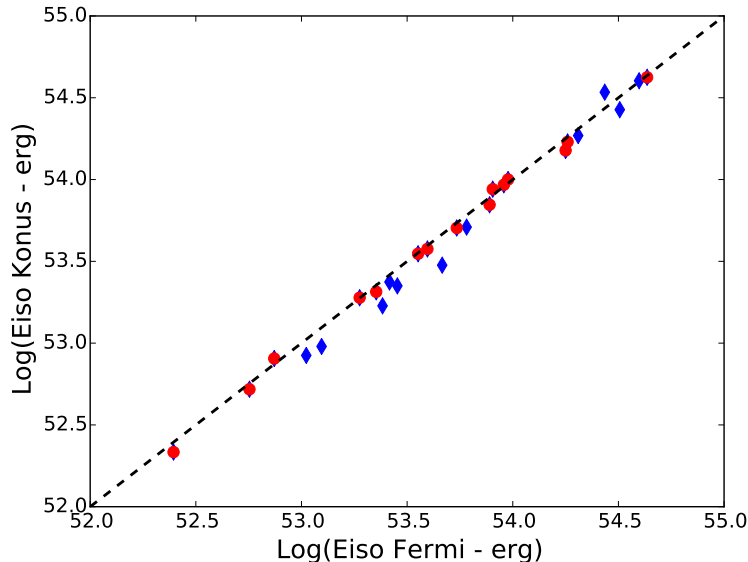


Figure 1. Comparison of E_{iso} measured by *Fermi*/GBM and *Konus-Wind* for 26 GRBs detected in common. The symbols refer to the model used for the spectral fit: red circles correspond to GRBs fitted with the same spectral model in *Konus-Wind* and *Fermi*/GBM, and blue diamonds to GRBs fitted with different spectral models. The 90% error bars have typically the size of the symbols. The dashed line indicates the equality of E_{iso} measured with *Fermi*/GBM and *Konus-Wind*.

For the purpose of this study, we construct two samples of long GRBs with reliable redshifts, fluence spectral parameters and homogeneous selection criteria. These samples are based on GRBs detected with *Fermi*/GBM (Meegan et al. 2009) and *Konus-Wind* (KW, Aptekar et al. 1995). These two instruments measure the spectral parameters of the prompt emission over a broad energy range, allowing reliable calculations of E_{iso} . For each instrument, we select long GRBs (with $T_{90} > 2$ s) according to the following criteria: a peak flux large enough to avoid detection threshold effects, a duration shorter than 1000 seconds and a best fit spectral model which is curved (i.e. not a simple power law). The isotropic energy release E_{iso} is calculated in the energy range $[1 - 10^4]$ keV in the cosmological rest-frame, following a standard procedure: we first compute the bolometric fluence in the energy range $[\frac{1}{1+z} - \frac{10^4}{1+z}]$ keV from the best fit fluence spectral model according to equation 1, then we compute E_{iso} from the bolometric fluence according to equation 2. $N(E)$ in equation 1 is the photon spectrum of the GRB, which is obtained from the best fit fluence spectrum in the *Fermi* GBM Burst Catalog for *Fermi* GRBs (Gruber et al. 2014; von Kienlin et al. 2014) and from the catalog of *Konus-Wind* bursts with known redshifts for *Konus* GRBs (Tsvetkova et al. 2017). The spectral parameters are listed in Tables 2 and 3. The ratio of integrals in equation 1, is the k-correction (Bloom et al. 2001), which is also listed in Tables 2 and 3.

$$S_{\text{bol}} = S_{\gamma} \frac{\int_{\frac{1}{1+z}}^{\frac{10^4}{1+z}} E N(E) dE}{\int_{E_{\text{min}}}^{E_{\text{max}}} E N(E) dE} \quad (1)$$

$$E_{\text{iso}} = \frac{4 \pi D_l^2 S_{\text{bol}}}{1+z} \quad (2)$$

Since we are mostly interested in energetic GRBs, which are rare in the local universe, we restrict our analysis to GRBs in the range $1 \leq z \leq 5$. This cut has two advantages: it limits the impact of redshift evolution within our sample and it avoids the complex optical selection effects taking place when the Lyman alpha forest enters the R band channel at $z \geq 6$. Moreover, since the volume enclosed within $z=1$ represents only 8% of the volume enclosed within $z=5$ we keep 92% of energetic GRBs, while removing from our sample low energy GRBs which are not useful for our analysis. Figure 2 shows the distribution in redshift and E_{iso} of the GRBs in our sample.

2.1.1. Peak flux and redshift selection

GRB samples in this study are subject to two selection effects: in peak flux and in redshift, the construction of a reliable energy distribution is only possible if we correctly take into account the impact of these selections. Considering

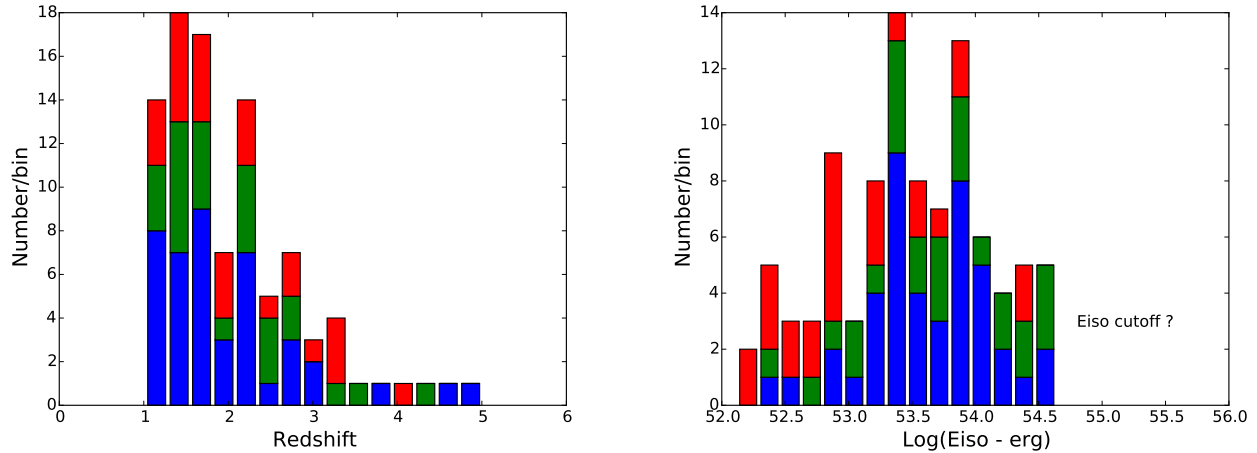


Figure 2. Histograms of redshift (left) and E_{iso} (right) of GRBs in this study. *Fermi*-only GRBs are indicated in red, *Konus*-only GRBs in blue, and GRBs detected by *Fermi* and *Konus* are indicated in green.

the selection of GRBs with a redshift, it has been shown by [Turpin et al. \(2016\)](#) that GRBs with small and large afterglow optical fluxes have similar distributions of E_{pi} (the maximum of the $\nu F\nu$ fluence spectrum), E_{iso} and L_{iso} (the isotropic equivalent luminosity). These authors conclude that the rest-frame distributions of E_{pi} , E_{iso} and L_{iso} are not significantly distorted when they are computed from GRBs with a redshift. We thus consider for the sake of this study that we do not bias the bright end of the GRB energy distribution when we study the distribution of GRBs with a redshift.

Considering the impact of peak flux selection, we construct GRB samples with a peak flux threshold in the trigger energy range that is typically 50% higher than the trigger threshold. This procedure transforms the complex detection instrument threshold into a well-defined *sample threshold*, at the expense of losing the faintest GRBs. The chosen values ensure that GRBs in our samples will be detected in most observing conditions. In the rest of this paper, we use the sample threshold to evaluate the impact of peak flux selection effects.

2.1.2. The *Fermi*/GBM sample

We construct the *Fermi*/GBM sample from the list of GRBs with a redshift provided in the online GRB table of Greiner², from August 2008 to mid-2016. The best fit spectral model is extracted from the *Fermi* GBM Burst Catalog ([Gruber et al. 2014](#); [von Kienlin et al. 2014](#)). In a first cut, we select GRBs with a 1-second peak flux larger than $P_f = 1.05 \text{ ph cm}^{-2} \text{ s}^{-1}$ in the energy range [50–300] keV. This is 1.5 times larger than the detection threshold of $0.7 \text{ ph cm}^{-2} \text{ s}^{-1}$ ([Narayana Bhat et al. 2016](#)). The requirement for a curved energy spectrum eliminates 6 GRBs whose best fit fluence spectrum is a power law. The duration cut eliminates one very long GRB (GRB 091024). After these cuts, we are left with a list of 52 GRBs given in Table 2.

The median 1-second peak flux of GRBs in our sample is $P_f = 2.45 \text{ ph cm}^{-2} \text{ s}^{-1}$ in the 50–300 keV energy range, and the median redshift $z=1.85$, which is smaller than the median redshift of *Swift* GRBs, $z=2.2$ ([Coward et al. 2013](#)).

2.1.3. The *Konus-Wind* sample

The *Konus-Wind* instrument collects GRB spectral data since 1994 over a wide energy range ($\sim 10 \text{ keV} - 10 \text{ MeV}$, nominally). In the period from 1997 January to mid-2016, KW detected ~ 150 GRBs with known redshifts in the triggered mode, of which 92 are in the range $1 \leq z \leq 5$. For details of the KW analysis and for the complete catalog of the KW bursts with known redshifts see [Tsvetkova et al. \(2017\)](#). We select here GRBs which have a 1-second peak flux larger than $P_f = 3.5 \text{ ph cm}^{-2} \text{ s}^{-1}$ in the energy range [50 – 200] keV and a duration shorter than 1000 seconds. The best fit fluence spectral model is chosen from the exponentially cutoff power-law (CPL) and the Band GRB function ([Band et al. 1993](#)) based on the difference in χ^2 between the fits. The criterion for accepting the Band function as the best-fit model is a χ^2 reduction of at least 6. We eliminate one GRB with a power law fluence spectrum. After these cuts, we are left with a list of 69 GRBs given in Table 3. The median 1-second peak flux of GRBs in our sample is $P_f = 7.3 \text{ ph cm}^{-2} \text{ s}^{-1}$ in the [50 – 200] keV energy range, and the median redshift $z=1.77$, which is again smaller than

² <http://www.mpe.mpg.de/~jcg/grbgen.html>

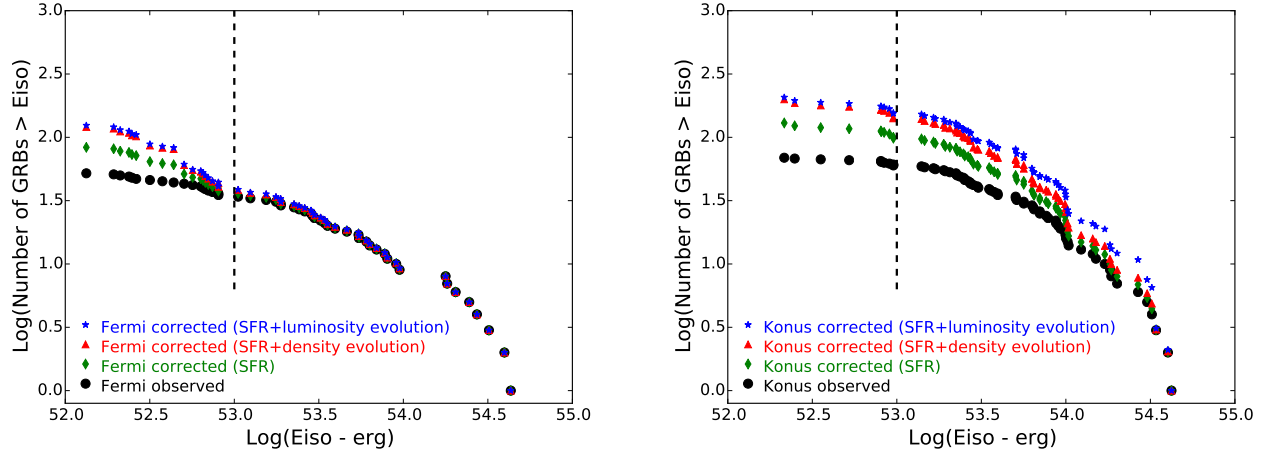


Figure 3. Cumulative distribution of GRB isotropic energy of 52 GRBs detected by *Fermi*/GBM (left panel) and 69 GRBs detected by *Konus-Wind* (right panel). The black circles show the observed distribution, while green diamonds, red triangles and blue stars respectively show the corrected distribution assuming that GRBs follow the SFR of [Hopkins & Beacom \(2006\)](#), the SFR multiplied by a density evolution proportional to $(1+z)^{1.6}$, or the SFR with E_{iso} evolution proportional to $(1+z)^{1.5}$. The smaller values of z_{max} for *Konus-Wind* lead to larger corrections on the right panel. The vertical dashed lines mark out GRBs with $E_{\text{iso}} \geq 10^{53}$ erg, which are studied in Section 3.

the median redshift of *Swift* GRBs, but comparable with the median redshift of the *Fermi* sample.

2.1.4. Comparison of the two samples

The *Fermi*/GBM and *Konus-Wind* samples contain 26 GRBs in common. Figure 1 compares E_{iso} measured with the *Fermi*/GBM and *Konus-Wind*. It evidences few facts: the two measurements agree within 25% for a large majority of GRBs (24/26); the agreement is better when the same model is used by the two instruments (red points); and in the few cases with a significant difference *Fermi* measures larger E_{iso} as demonstrated by the location of the majority of the blue points below the dashed line. The good agreement on E_{iso} measured with two instruments with different energy thresholds and different methods of spectral analyses indicate that the two samples used in this study are reliable, with no strong systematic uncertainties.

The largest differences reach 30% for GRB 081222 ($E_{\text{iso}} = 2.4 \times 10^{53}$ erg for *Fermi*/GBM vs $E_{\text{iso}} = 1.7 \times 10^{53}$ erg for *Konus-Wind*), and 35% for GRB 110731A ($E_{\text{iso}} = 4.6 \times 10^{53}$ erg for *Fermi*/GBM vs $E_{\text{iso}} = 3.0 \times 10^{53}$ erg for *Konus-Wind*). We note that these differences reduce to 21% and 30% respectively when the same model is used to fit the spectra from the two instruments. These differences do not impact the analysis presented here, which is based on the number of GRBs found in broad classes of luminosity (0.5 dex, corresponding to a factor 3).

Three GRBs detected in common have durations that differ by more than a factor two between *Fermi*/GBM and *Konus-Wind* (GRB 081121, GRB 160509A, GRB 160625B), however the fluences measured by the two instruments differ by less than 5%, validating the measure of E_{iso} .

2.2. The corrected E_{iso} distribution

Figure 3 shows with black circles the observed cumulative distribution of E_{iso} for *Fermi*/GBM and *Konus-Wind* GRBs. These distributions do not represent the true GRB energy distribution since many GRBs are not detectable within the entire volume under study ($1 \leq z \leq 5$). In order to construct the true E_{iso} distribution, we use a two step procedure correcting for the detection inefficiency of GRBs in our samples. First, we compute for each GRB the maximum distance at which its peak flux stays above the peak flux threshold of the sample. This “GRB horizon”, z_{max} is given in Tables 2 and 3. For bright GRBs visible to distances larger than $z = 5$, we set the horizon to $z = 5$, which is the redshift limit of our samples. Tables 2 and 3 allow comparing the “horizon” of *Fermi*/GBM and *Konus-Wind* for GRBs detected in common. Unlike E_{iso} , we find some differences here (e.g. GRB 120624B which is detectable to $z_{\text{max}} = 2.92$ with *Konus-Wind* and to $z_{\text{max}} = 5.0$ with *Fermi*/GBM). These differences are readily explained by the different sensitivities of the two instruments which led us to adopt different peak flux thresholds for the two samples, as explained in section 2.1.1. The calculation of z_{max} permits taking this parameter into account in our analysis.

In a second step we compute a “weight” for each GRB, given by the ratio of the number of GRBs of this type within $z = 5$ to the number of GRBs within z_{max} . With this method, bright GRBs visible out to $z = 5$ will be given a weight

of 1, while fainter GRBs with an horizon smaller than $z = 5$ will be given a weight larger than 1. The weight of a GRB is thus the inverse of its detection efficiency within the volume under study.

The calculation of these weights require a GRB world model, which describes the volume density evolution and the energy evolution of GRBs with redshift. For the purpose of this paper, which aims at studying the bright end of the energy distribution in a restricted range of redshift, we have limited our analysis to three simple cases. First, a model with no evolution, where the number of GRBs is proportional to the Star Formation Rate (SFR) proposed by [Hopkins & Beacom \(2006\)](#) and [Li \(2008\)](#). This model is described by equations 3 and 4, and it leads to the weights labeled W_{sfr} . Second, a model with density evolution described by equation 5 with $\delta_n = 1.6$, leading to the weights labeled W_d . Third, a model with luminosity evolution described by equation 6 with $\delta_l = 1.5$. Apart from GRBs visible out to $z=5$, which have weight unity, the weights of other GRBs depend on the model. For models with luminosity evolution, the weights also depend on the luminosity function, the weights labeled W_{pl} refer to GRBs with a power law energy function, while W_{cpl} refer to GRBs with a cutoff power law energy function. The indices for the density and luminosity evolution are typical values inferred from recent studies (e.g. [Kistler et al. 2008](#); [Salvaterra et al. 2012](#); [Howell et al. 2014](#); [Petrosian et al. 2015](#); [Tan & Wang 2015](#)). Equations 3, 4, 5, 6 give the formulae used for the calculation of the Star Formation Rate (equations 3) and for the calculation of the number of GRBs closer than redshift z_a , $N(< z_a)$, for three cases of redshift evolution (equations 4, 5, 6).

$$SFR(z) \propto \frac{0.0157 + 0.118z}{1 + (\frac{z}{3.23})^{4.66}} \quad (3)$$

$$N(< z_a) \propto \int_0^{z_a} SFR(z) \frac{1}{(1+z)} \frac{dV(z)}{dz} dz \quad - \quad \text{no evolution} \quad (4)$$

$$N(< z_a) \propto \int_0^{z_a} SFR(z) \frac{1}{(1+z)} \frac{dV(z)}{dz} (1+z)^{\delta_n} dz \quad - \quad \text{density evolution} \quad (5)$$

$$N(< z_a) \propto \int_0^{z_a} SFR(z) \frac{1}{(1+z)} \frac{dV(z)}{dz} \frac{\phi(\frac{L}{(1+z)^{\delta_l}})}{\phi(L)} dz \quad - \quad \text{luminosity evolution} \quad (6)$$

For the density evolution model, the GRB rate is multiplied by nearly a factor six from redshift one to redshift five compared to the no evolution scenario. For the luminosity evolution model, the GRB energy increases by about a factor five from redshift one to redshift five. In this model, the increase of the GRB rate with the redshift depends on the energy of the GRBs and on the shape of the energy distribution.

Tables 2 and 3 give the weights of GRBs for the different GRB world models studied here. They show that the models with density or luminosity evolution have larger weights and require larger corrections because the comoving GRB density increases faster with redshift, leading to a higher fraction of undetected bursts for the same z_{max} .

Having the weight of each GRB in our sample, we can then compute the corrected E_{iso} distribution. Figure 3 shows with green diamonds the corrected distributions for a model with no evolution, with red triangles the corrected distributions for the model with density evolution, and with blue stars the corrected distributions for a model with luminosity evolution. The left panel shows the energy distributions derived from *Fermi*/GBM observations and the right panel those derived from (less sensitive) *Konus-Wind* observations. The corrected E_{iso} distributions, like the observed one, exhibit a break around $E_{\text{iso}} = 1 - 3 \times 10^{54}$ erg, which is the topic of this paper.

Table 2. Table of 52 GRBs detected by *Fermi*/GBM used in this study. The 12 columns give respectively the name of the GRB, its duration T_{90} , its fluence in the $[10 - 10^3]$ keV energy range, the parameters of the fluence spectral model, the redshift and k-correction (Bloom et al. 2001), E_{iso} , z_{max} , and the weights of the GRBs for the four models under study (see section 2.2). The spectral parameters and the names of the spectral models are taken from the *Fermi* GBM Burst Catalog (Gruber et al. 2014; von Kienlin et al. 2014). For the COMP model, the two parameters in the table are E_{peak} in keV and the power law index. For the BAND model, the three parameters in the table are E_{peak} in keV, the low energy power law index and the high energy power law index. For the SBPL model, the three parameters in the table are the smoothly broken power law break energy in keV, the low energy power law index and the high energy power law index. The errors on E_{iso} have been derived from the error on the fluence, according to equations 1 and 2. GRBs detected in common with Konus are indicated in bold.

GRB	T_{90} s	$S_{\gamma}/10^{-7}$ erg.cm $^{-2}$	Spectral model	z	k-cor.	$E_{\text{iso}}/10^{52}$ erg	z_{max}	W_{sfr}	W_{d}	W_{pl}	W_{cpl}
GRB080804972	24.7	91	SBPL 109 -0.70 -1.93	2.20	1.48	15.4 ± 0.30	3.06	1.37	1.76	2.07	1.81
GRB080810549	107.5	108	COMP 855 -1.18	3.35	1.37	34.3 ± 0.25	3.39	1.23	1.48	1.68	1.53
GRB080916009	63.0	603	SBPL 302 -1.14 -2.09	4.35	1.52	272.5 ± 0.52	5.00	1.00	1.00	1.00	1.00
GRB081121858	42.0	153	BAND 161 -0.43 -2.09	2.51	1.52	28.4 ± 0.68	5.00	1.00	1.00	1.00	1.00
GRB081221681	29.7	300	COMP 88 -0.91	2.26	1.52	39.4 ± 0.19	5.00	1.00	1.00	1.00	1.00
GRB081222204	18.9	119	BAND 143 -0.86 -2.31	2.77	1.52	24.2 ± 0.32	5.00	1.00	1.00	1.00	1.00
GRB090102122	26.6	279	COMP 417 -0.94	1.55	1.52	18.8 ± 0.07	4.15	1.07	1.15	1.22	1.16
GRB090113778	17.4	16	COMP 178 -1.28	1.75	1.12	1.3 ± 0.07	2.26	2.21	3.49	4.65	3.58
GRB090323002	135.2	1181	SBPL 345 -1.34 -2.27	3.57	1.52	396.2 ± 0.96	5.00	1.00	1.00	1.00	1.00
GRB090516353	123.1	172	COMP 164 -1.54	4.11	1.26	69.4 ± 0.37	4.37	1.05	1.10	1.14	1.12
GRB090902462	19.3	2218	SBPL 1170 -1.09 -4.85	1.82	1.36	245.3 ± 0.58	5.00	1.00	1.00	1.00	1.00
GRB090926181	13.8	1466	SBPL 202 -0.98 -2.31	2.11	1.52	203.9 ± 0.78	5.00	1.00	1.00	1.00	1.00
GRB090926914	55.6	108	COMP 86 0.04	1.24	1.02	4.4 ± 0.10	1.36	9.35	20.48	32.65	21.61
GRB091020900	24.3	83	COMP 244 -1.26	1.71	1.11	6.7 ± 0.20	2.70	1.62	2.26	2.79	2.32
GRB091208410	12.5	62	COMP 127 -1.34	1.06	1.16	2.1 ± 0.11	2.49	1.84	2.73	3.49	2.79
GRB100414097	26.5	885	COMP 668 -0.63	1.37	1.52	54.3 ± 0.19	4.58	1.03	1.06	1.08	1.07
GRB100615083	37.4	87	COMP 144 -1.35	1.40	1.16	5.0 ± 0.08	1.96	3.01	5.27	7.43	5.48
GRB100728095	165.4	1279	BAND 290 -0.64 -2.70	1.57	1.52	95.0 ± 0.71	3.93	1.10	1.22	1.31	1.27
GRB100728439	10.2	33	COMP 160 -0.98	2.11	1.06	3.8 ± 0.12	2.88	1.48	1.97	2.38	2.01
GRB100814160	150.5	149	COMP 156 -0.50	1.44	1.02	8.1 ± 0.08	2.39	1.98	3.01	3.92	3.11
GRB100906576	110.6	233	SBPL 27 -0.89 -1.86	1.73	1.52	26.1 ± 0.11	3.89	1.11	1.23	1.33	1.25
GRB110213220	34.3	94	COMP 113 -1.57	1.46	1.29	6.5 ± 0.06	2.61	1.71	2.44	3.06	2.51
GRB110731465	7.5	229	SBPL 287 -1.04 -2.96	2.83	1.52	46.3 ± 0.19	5.00	1.00	1.00	1.00	1.00
GRB120119170	55.3	387	BAND 183 -0.96 -2.37	1.73	1.52	35.6 ± 0.21	4.46	1.04	1.08	1.12	1.09
GRB120326056	11.8	33	SBPL 31 -0.92 -2.40	1.80	1.22	3.2 ± 0.08	2.27	2.18	3.44	4.57	3.54
GRB120624933	271.4	1916	SBPL 358 -1.02 -2.23	2.20	1.52	320.9 ± 0.55	5.00	1.00	1.00	1.00	1.00
GRB120711115	44.0	1943	BAND 1319 -0.98 -2.80	1.41	1.52	181.7 ± 0.35	5.00	1.00	1.00	1.00	1.00
GRB120716712	237.1	144	BAND 85 -0.76 -1.84	2.49	1.43	29.1 ± 0.14	4.24	1.06	1.13	1.18	1.14
GRB120811649	14.3	34	COMP 61 -0.93	2.67	1.16	6.3 ± 0.64	3.18	1.31	1.64	1.90	1.66
GRB121128212	17.3	93	SBPL 43 -0.91 -2.48	2.20	1.52	12.4 ± 0.25	4.78	1.01	1.03	1.04	1.03
GRB130518580	48.6	946	BAND 398 -0.91 -2.25	2.49	1.52	177.8 ± 0.48	5.00	1.00	1.00	1.00	1.00
GRB131011741	77.1	89	COMP 274 -0.96	1.87	1.06	8.1 ± 0.10	2.68	1.64	2.30	2.86	2.37
GRB131105087	112.6	238	COMP 266 -1.26	1.69	1.12	18.8 ± 0.14	3.04	1.38	1.77	2.09	1.83
GRB131108862	18.2	357	SBPL 240 -1.04 -2.42	2.40	1.52	60.5 ± 0.38	5.00	1.00	1.00	1.00	1.00
GRB140206304	27.3	155	BAND 121 0.06 -2.35	2.73	1.16	29.8 ± 0.24	5.00	1.00	1.00	1.00	1.00
GRB140213807	18.6	212	BAND 87 -1.13 -2.26	1.21	1.52	10.5 ± 0.05	2.90	1.47	1.95	2.34	2.00
GRB140423356	95.2	181	BAND 121 -0.58 -1.83	3.26	1.36	54.6 ± 0.61	3.84	1.12	1.25	1.35	1.29
GRB140508128	44.3	614	BAND 263 -1.19 -2.36	1.03	1.52	22.6 ± 0.07	5.00	1.00	1.00	1.00	1.00

Table 2 continued on next page

Table 2 (*continued*)

GRB	T ₉₀ s	S _γ /10 ⁻⁷ erg.cm ⁻²	Spectral model	z	k-cor.	E _{iso} /10 ⁵² erg	z _{max}	W _{sfr}	W _d	W _{pl}	W _{cpl}
GRB140620219	45.8	61	COMP 127 -1.28	2.04	1.14	7.0 ± 0.12	2.57	1.75	2.52	3.18	2.59
GRB140703026	84.0	76	COMP 221 -1.28	3.14	1.12	17.6 ± 0.20	4.23	1.06	1.13	1.18	1.14
GRB140801792	7.2	124	COMP 121 -0.40	1.32	1.52	5.7 ± 0.03	3.44	1.22	1.45	1.62	1.46
GRB140808038	4.5	32	COMP 123 -0.47	3.29	1.52	7.4 ± 0.12	5.00	1.00	1.00	1.00	1.00
GRB140907672	35.8	65	COMP 142 -1.03	1.21	1.08	2.6 ± 0.04	1.45	7.39	15.66	24.53	16.38
GRB141028455	31.5	348	BAND 294 -0.84 -1.97	2.33	1.44	63.2 ± 0.27	5.00	1.00	1.00	1.00	1.00
GRB141220252	7.6	53	COMP 178 -0.82	1.32	1.52	2.5 ± 0.03	2.97	1.42	1.86	2.21	1.89
GRB141221338	23.8	41	COMP 182 -1.18	1.45	1.09	2.4 ± 0.06	2.01	2.83	4.87	6.80	5.03
GRB150301818	13.3	31	COMP 226 -1.12	1.52	1.08	1.9 ± 0.03	1.88	3.31	5.94	8.50	6.14
GRB150314205	10.7	816	BAND 347 -0.68 -2.60	1.76	1.52	77.7 ± 0.20	5.00	1.00	1.00	1.00	1.00
GRB150403913	22.3	547	BAND 429 -0.87 -2.11	2.06	1.52	80.4 ± 0.13	5.00	1.00	1.00	1.00	1.00
GRB160509374	369.7	1790	BAND 355 -1.02 -2.23	1.17	1.52	90.7 ± 0.13	5.00	1.00	1.00	1.00	1.00
GRB160625945	454.7	5692	BAND 649 -0.95 -2.37	1.41	1.52	432.2 ± 1.19	5.00	1.00	1.00	1.00	1.00
GRB160629930	64.8	131	COMP 291 -1.03	3.33	1.07	32.4 ± 0.14	5.00	1.00	1.00	1.00	1.00

Table 3. Table of 69 GRBs detected by *Konus-Wind* used in this study. The 12 columns give respectively the name of the GRB, its duration T_{90} , its fluence in the $[10 - 10^4]$ keV energy range, the parameters of the fluence spectral model, the redshift and k-correction (Bloom et al. 2001), E_{iso} , z_{max} , and the weights of the GRBs for the four models under study (see section 2.2). The GRB parameters have been extracted from the *Konus-WIND* catalog of GRBs with known redshifts (Tsvetkova et al. 2017). For the COMP model, the two parameters in the table are E_{peak} in keV and the power law index. For the BAND model, the three parameters in the table are E_{peak} in keV, the low energy power law index and the high energy power law index. The errors on E_{iso} have been derived from the error on the fluence, according to equations 1 and 2. GRBs detected in common with *Fermi*/GBM are indicated in bold.

GRB	T_{90} s	$S_{\gamma}/10^{-7}$ erg.cm $^{-2}$	Spectral model	z	k-cor.	$E_{\text{iso}}/10^{52}$ erg	z_{max}	W_{sfr}	W_{d}	W_{pl}	W_{cpl}
GRB990123	62.0	2320	COMP 724 -0.94	1.60	1.35	201.0 ± 8.50	4.01	1.09	1.19	1.19	1.23
GRB990506	128.6	1600	BAND 296 -1.19 -2.09	1.31	1.47	103.8 ± 5.75	2.58	1.74	2.50	2.43	2.65
GRB990510	55.9	216	COMP 136 -1.35	1.62	1.16	16.5 ± 1.12	2.25	2.22	3.52	3.40	3.46
GRB991216	14.5	1956	BAND 353 -1.20 -2.23	1.02	1.44	76.5 ± 1.60	3.67	1.15	1.32	1.31	1.33
GRB000131	96.5	337	BAND 133 -0.90 -2.26	4.50	1.16	144.3 ± 6.99	5.00	1.00	1.00	1.00	1.00
GRB000418	27.8	218	COMP 116 -1.56	1.12	1.27	9.0 ± 0.60	1.51	6.32	13.06	12.42	12.63
GRB000911	23.4	1071	BAND 1083 -0.82 -2.75	1.06	1.80	56.4 ± 2.93	1.64	4.82	9.48	9.04	9.99
GRB000926	54.7	209	COMP 108 -1.51	2.04	1.27	26.4 ± 1.21	2.44	1.91	2.86	2.78	2.84
GRB010222	89.8	1154	BAND 285 -1.26 -2.17	1.48	1.41	90.1 ± 4.06	2.95	1.43	1.88	1.85	1.95
GRB020813	89.4	1191	BAND 227 -0.90 -2.24	1.25	1.35	64.8 ± 6.74	2.58	1.73	2.50	2.43	2.56
GRB050401	33.1	182	BAND 105 -0.82 -2.31	2.90	1.19	39.5 ± 2.74	3.72	1.14	1.30	1.29	1.30
GRB050603	11.2	265	BAND 239 -0.69 -1.94	2.82	1.39	64.1 ± 6.49	5.00	1.00	1.00	1.00	1.00
GRB051008	208.8	385	COMP 550 -0.98	2.77	1.21	78.7 ± 11.97	3.25	1.28	1.58	1.56	1.61
GRB060124	78.1	202	COMP 239 -1.17	2.30	1.09	27.1 ± 2.31	2.88	1.48	1.97	1.93	1.96
GRB061007	57.6	1863	BAND 399 -0.70 -2.61	1.26	1.30	99.0 ± 5.95	2.74	1.58	2.18	2.13	2.28
GRB061121	17.8	486	COMP 607 -1.32	1.31	1.32	28.4 ± 1.76	2.90	1.46	1.94	1.90	1.93
GRB061222	60.2	225	COMP 298 -0.89	2.09	1.06	24.7 ± 1.06	2.85	1.50	2.01	1.97	2.00
GRB070125	124.2	1146	BAND 372 -1.10 -2.09	1.55	1.48	102.4 ± 8.42	3.26	1.28	1.57	1.55	1.62
GRB070328	53.8	370	BAND 386 -0.80 -2.00	2.06	1.50	56.3 ± 10.37	2.21	2.30	3.70	3.57	3.81
GRB070521	31.8	186	COMP 218 -0.92	1.70	1.05	14.0 ± 0.71	2.03	2.78	4.74	4.57	4.65
GRB071003	21.4	396	COMP 801 -0.97	1.60	1.41	35.9 ± 2.86	2.24	2.24	3.57	3.46	3.60
GRB071020	2.7	71	COMP 322 -0.65	2.15	1.04	8.1 ± 1.15	2.98	1.41	1.84	1.80	1.81
GRB071117	2.3	63	COMP 278 -1.53	1.33	1.24	3.5 ± 0.36	2.11	2.54	4.21	4.07	4.08
GRB080319	10.2	121	COMP 632 -1.21	1.95	1.31	14.6 ± 2.72	2.09	2.59	4.33	4.18	4.25
GRB080411	42.8	660	COMP 266 -1.52	1.03	1.23	22.5 ± 1.14	2.15	2.44	4.00	3.87	3.97
GRB080514	5.7	262	BAND 196 -0.53 -2.46	1.80	1.21	25.2 ± 1.87	4.19	1.07	1.14	1.14	1.14
GRB080603	12.6	51	COMP 101 -1.21	2.69	1.15	9.5 ± 2.33	2.90	1.46	1.94	1.90	1.91
GRB080605	13.7	323	COMP 260 -0.89	1.64	1.05	22.7 ± 0.73	3.51	1.20	1.41	1.39	1.40
GRB080607	28.7	766	BAND 334 -0.71 -2.52	3.04	1.21	182.4 ± 8.04	5.00	1.00	1.00	1.00	1.00
GRB080721	19.7	625	BAND 490 -0.93 -2.45	2.59	1.31	123.1 ± 8.53	5.00	1.00	1.00	1.00	1.00
GRB080916	61.3	788	BAND 505 -1.04 -2.26	4.35	1.24	341.8 ± 45.47	5.00	1.00	1.00	1.00	1.00
GRB081121	19.4	151	COMP 254 -0.79	2.51	1.04	22.4 ± 1.62	2.59	1.72	2.47	2.40	2.45
GRB081221	29.2	278	COMP 81 -1.03	2.26	1.13	37.6 ± 1.22	3.21	1.30	1.61	1.58	1.61
GRB081222	12.0	96	COMP 192 -0.84	2.77	1.04	16.9 ± 1.92	3.13	1.33	1.68	1.65	1.67
GRB090102	15.3	279	COMP 432 -0.90	1.55	1.12	19.0 ± 1.65	1.86	3.40	6.16	5.91	6.07
GRB090201	67.3	730	BAND 156 -0.90 -2.71	2.10	1.14	87.5 ± 4.04	3.68	1.15	1.32	1.30	1.34
GRB090323	133.0	1187	BAND 417 -0.96 -2.10	3.60	1.30	401.7 ± 51.76	4.72	1.02	1.04	1.04	1.05
GRB090709	77.3	755	COMP 277 -0.86	1.80	1.05	63.0 ± 1.94	2.43	1.93	2.89	2.81	2.98
GRB090926	13.2	1438	BAND 327 -0.79 -2.61	2.11	1.22	185.6 ± 7.70	5.00	1.00	1.00	1.00	1.00

Table 3 continued on next page

Table 3 (*continued*)

GRB	T_{90} s	$S_{\gamma}/10^{-7}$ erg.cm $^{-2}$	Spectral model	z	k-cor.	$E_{\text{iso}}/10^{52}$ erg	z_{max}	W_{sfr}	W_{d}	W_{pl}	W_{cpl}
GRB100414	21.7	888	COMP 571 -0.49	1.37	1.19	50.6 ± 1.68	2.09	2.59	4.32	4.17	4.43
GRB100606	59.1	306	COMP 874 -1.00	1.55	1.47	27.3 ± 3.48	1.59	5.35	10.73	10.22	10.74
GRB100728	159.9	1270	BAND 305 -0.65 -2.48	1.57	1.27	100.1 ± 10.21	2.01	2.81	4.82	4.64	5.30
GRB100906	90.1	249	COMP 195 -1.60	1.73	1.28	23.6 ± 4.29	2.00	2.86	4.94	4.75	4.90
GRB110422	22.3	844	BAND 155 -0.70 -3.21	1.77	1.08	70.1 ± 1.73	4.36	1.05	1.10	1.10	1.11
GRB110503	6.7	253	BAND 220 -0.98 -2.71	1.61	1.18	19.3 ± 1.43	3.51	1.20	1.41	1.39	1.40
GRB110731	6.7	164	COMP 288 -0.74	2.83	1.04	30.0 ± 1.89	4.05	1.08	1.18	1.17	1.18
GRB111008	12.7	70	COMP 104 -1.53	5.00	1.30	39.5 ± 8.83	5.00	1.00	1.00	1.00	1.00
GRB120119	39.6	383	BAND 153 -0.85 -2.34	1.73	1.24	35.2 ± 4.15	2.44	1.91	2.87	2.79	2.88
GRB120624	267.9	1911	COMP 560 -1.04	2.20	1.23	267.3 ± 18.69	2.92	1.45	1.92	1.88	2.22
GRB120711	41.3	1979	BAND 1061 -0.97 -2.71	1.41	1.69	169.9 ± 6.49	2.43	1.92	2.88	2.80	3.28
GRB121128	10.0	74	COMP 77 -0.99	2.20	1.13	9.5 ± 0.46	3.03	1.38	1.78	1.75	1.76
GRB130408	4.2	75	BAND 271 -0.70 -2.30	3.76	1.20	25.2 ± 8.80	4.32	1.05	1.11	1.11	1.11
GRB130505	14.7	1580	BAND 593 -0.49 -2.04	2.27	1.59	302.6 ± 11.52	5.00	1.00	1.00	1.00	1.00
GRB130518	28.6	740	BAND 332 -0.88 -1.96	2.49	1.44	150.6 ± 15.98	5.00	1.00	1.00	1.00	1.00
GRB130701	3.7	63	COMP 89 -1.10	1.16	1.13	2.5 ± 0.12	1.78	3.85	7.19	6.88	6.91
GRB130907	180.3	5594	BAND 387 -0.90 -2.22	1.24	1.45	322.6 ± 17.98	2.99	1.41	1.83	1.80	2.16
GRB131030	15.7	647	BAND 196 -0.52 -3.05	1.29	1.10	30.3 ± 1.98	2.93	1.45	1.91	1.87	1.90
GRB131108	17.7	343	COMP 358 -1.16	2.40	1.13	51.2 ± 3.83	3.63	1.16	1.34	1.33	1.35
GRB140213	16.4	183	COMP 100 -1.40	1.21	1.21	8.4 ± 0.29	1.91	3.18	5.65	5.43	5.49
GRB140508	149.7	594	BAND 220 -1.17 -2.54	1.03	1.25	20.6 ± 2.34	2.85	1.50	2.02	1.98	2.00
GRB140801	6.2	113	COMP 108 -0.44	1.32	1.03	5.2 ± 0.19	1.65	4.72	9.24	8.82	8.90
GRB140808	5.2	33	COMP 125 -0.94	3.29	1.07	8.0 ± 0.76	3.47	1.21	1.43	1.41	1.41
GRB141220	6.9	47	COMP 139 -0.55	1.32	1.03	2.2 ± 0.18	1.49	6.64	13.84	13.16	13.21
GRB150206	35.1	370	BAND 228 -0.73 -2.20	2.09	1.31	50.5 ± 6.15	3.18	1.31	1.64	1.62	1.65
GRB150314	10.2	775	BAND 350 -0.78 -2.90	1.76	1.18	70.1 ± 3.25	5.00	1.00	1.00	1.00	1.00
GRB150403	21.0	595	BAND 373 -0.93 -2.06	2.06	1.45	87.3 ± 7.74	4.43	1.04	1.09	1.08	1.09
GRB151021	57.0	650	BAND 170 -1.14 -2.46	2.33	1.22	99.5 ± 14.22	3.05	1.38	1.77	1.74	1.83
GRB160509	28.5	1749	BAND 288 -0.99 -2.08	1.17	1.50	92.9 ± 14.02	3.17	1.32	1.65	1.62	1.69
GRB160625	21.0	5473	BAND 571 -0.80 -2.28	1.41	1.52	421.5 ± 8.49	5.00	1.00	1.00	1.00	1.00

3. THE MOST ENERGETIC GRBS

In this section we compare the distribution of E_{iso} derived above with two models of the energy function: a simple power law (more correctly called the Pareto distribution) and a power law with a high energy cutoff (more correctly called the gamma distribution). Our goal is to assess the significance of the energy cutoff observed in figure 3.

Combining these two energy functions with the three GRB world models previously discussed (SFR, SFR+density evolution, SFR+luminosity evolution), we obtain a total of six models, that are compared with the data thanks to a chisquare test. For the purpose of the test, we classify GRBs into 5 classes of E_{iso} ranging from 10^{53} to 10^{56} erg. Within each class of E_{iso} we compute the number of GRBs predicted by the theoretical model, taking into account a detection efficiency defined as the average weight of GRBs in this class, and we compare the theoretical numbers with the observed numbers.

The comparison involves the normalization of the theoretical numbers to the number of observed GRBs with energies larger than 10^{53} erg: 59 for *Konus-Wind*, and 34 for *Fermi/GBM*, and we use the predicted numbers for the variance term in the denominator. Since the weights of the GRBs are directly computed from the models (equations 4 to 6), this procedure permits the comparison of an observed quantity, the number of GRBs in each class, with the theoretical prediction of each model. We have restricted our analysis to GRBs with $E_{\text{iso}} \geq 10^{53}$ erg, because they have weights which are not too large, indicating that we detect a significant fraction of the GRB population at these energies. Table 4 gives the observed and predicted number of GRBs in each class and the mean weight of GRBs within each energy

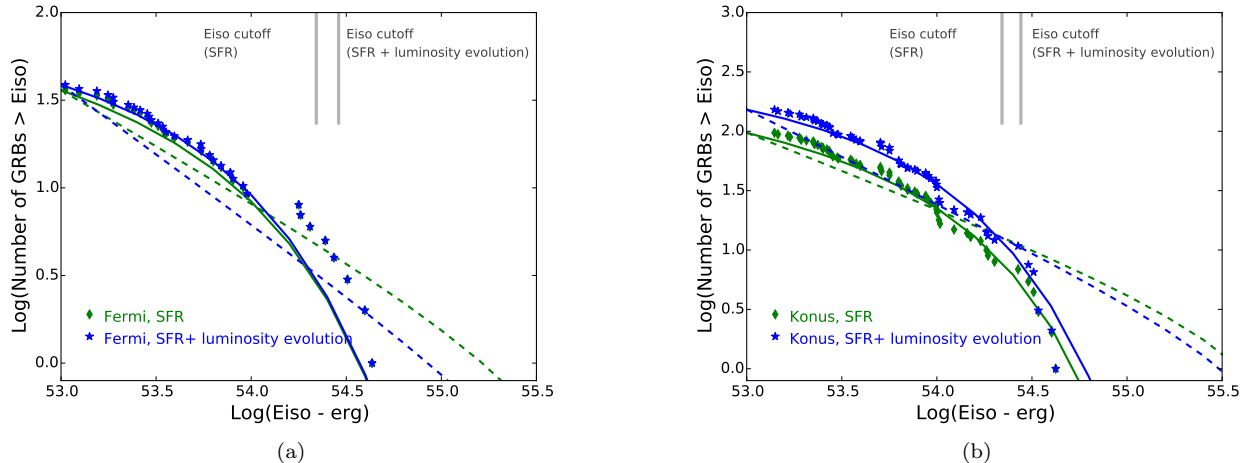


Figure 4. Comparison of the best fit power law (dashed line) and of the best fit cutoff power law (solid line) E_{iso} distributions with the distributions measured by *Fermi* (left) and *Konus* (right). We have plotted the best fit distributions for the *Konus* sample because they are more constrained. The grey vertical lines show the cutoff energy derived in Table 4, for the luminosity evolution model, the cutoff changes with the redshift, and we have plotted the cutoff energy at the median redshift of the sample ($z=1.85$ for *Fermi*/GBM and $z=1.77$ for *Konus-Wind*). The symbols are the same as in Figure 3.

class. The parameters of the best fit energy function are obtained with a minimization of the chisquare.³

Considering the power law fits, our analysis gives slopes that are compatible with previous works involving a power law luminosity function at high luminosity or high energy. The value found here ($\gamma = -1.6 \pm 0.25$) is compatible with the values obtained by [Wanderman & Piran \(2010\)](#) ($\gamma = -1.4^{+0.6}_{-0.3}$), [Salvaterra et al. \(2012\)](#) ($\gamma = -2.3^{+0.3}_{-0.8}$ for density evolution and $\gamma = -1.9^{+0.11}_{-0.14}$ for luminosity evolution), [Howell et al. \(2014\)](#) ($\gamma = -2.59 \pm 0.93$), or [Pescalli et al. \(2015\)](#) ($\gamma = -1.84 \pm 0.24$), for instance. On the other hand, Table 4 shows that the choice of a cutoff PL model leads to a shallower slope of the energy distribution ($\gamma \sim -0.9$ to -1.1 vs $\gamma \sim -1.6$).

Our main point concerns the comparison of the simple power law energy distribution with the cutoff power law energy distribution. Table 4 shows that the addition of the cutoff improves the fit, only slightly for the *Fermi* sample, but significantly for the *Konus-Wind* sample. We attribute the larger improvement measured for *Konus-Wind* to the larger number of energetic GRBs in the *Konus-Wind* sample: 59 GRBs with $E_{\text{iso}} \geq 10^{53}$ erg, versus 34 for the *Fermi* sample, which leads to larger numbers of GRBs in the energy classes. Since the only difference between the two models is the addition of one free parameter (the cutoff energy), the chisquare difference follows a chisquare law with one degree of freedom, allowing measuring the significance of the improvement. The chisquare difference $\Delta\chi \geq 10$ measured for the *Konus-Wind* sample shows that the energy cutoff is required at a level larger than **99.8%**. We stress that the need for the GRB energy cutoff does not depend on the GRB world model, as shown by the chisquare values in Table 4. This result is illustrated in Figure 4, which compares the best fit energy distributions with the distribution of E_{iso} observed by *Konus* for four of the six models studied here.

In order to assess the physical reality of the cutoff, we have checked that it is not due to an instrumental effect. The instrumental dead time could produce a saturation of the measured flux due to the loss of photons during very bright peaks exceeding 10^5 cts/sec on the detector. However, this effect cannot explain a saturation of the energy, which is an intrinsic GRB property. Specifically, we have checked that the most energetic GRBs in our samples are not specially bright in the observer frame (see Figure 5 panel f): the six *Fermi* GRBs (resp. *Konus-Wind* GRBs) with $E_{\text{iso}} > 2.3 \times 10^{54}$ erg have the following rank in term of their observed peak photon flux: 1-26-20-8-24-3 (resp. 47-55-50-4-11-1). Given the count rates of these bursts, the measurements of their E_{iso} are not affected by significant dead time effects. Since there is no mechanism that could prevent the detection of very energetic GRBs or affect strongly the measurement of E_{iso} , we conclude that the energy cutoff of the gamma-ray isotropic emission at $1 - 3 \times 10^{54}$ erg is an intrinsic property of the sources.

We also checked the energy of GRBs outside the redshift range considered here. The most energetic GRB below

³ For the power law fits, we have also indicated the best fit parameters that maximize the likelihood function, showing the consistency with the chi-square analysis.

$z=1$ is GRB 110918A at $z=0.984$, with $E_{\text{iso}} = 2.3 \times 10^{54}$ erg measured by *Konus-Wind*, (Frederiks et al. 2013). The extremely bright GRB 130427A located at $z=0.34$ stands a factor three below the limit, with $E_{\text{iso}} = 8 \times 10^{53}$ erg (e.g. Ackermann et al. 2014; Maselli et al. 2014; Perley et al. 2014; Vestrand et al. 2014). The most energetic GRB above $z=5$ is GRB 130606A at $z=5.913$, with $E_{\text{iso}} = 2.7 \times 10^{53}$ erg measured by *Konus-Wind*, (Golenetskii et al. 2013) a factor ten below the limit discussed here. Thus, GRBs outside the redshift range $[1-5]$ do not exceed the energy limit derived from GRBs with redshift in this range.

We finally note that ultra-long GRBs (e.g. Gendre et al. 2013; Levan et al. 2014), do not exceed the energy limit discussed here despite their long duration. GRB 111209A for instance has $E_{\text{iso}} = 6 \times 10^{53}$ erg, four times below the cutoff energy.

Table 4. Comparison of the observed number of GRBs with the predictions of six models. Column 1 describes the GRB world model. Columns 2 to 6 give the observed and predicted number of GRBs in 5 energy classes. Columns 7 and 8 give the parameters of the best fit energy function, based on chi-square minimization (upper row) and on maximum likelihood (lower row, only for the power law distribution). For models with luminosity evolution, the parameters correspond to the energy function at redshift $z=0$. Column 9 indicates the agreement between the observed and predicted number of GRB based on a chi-square test. Column 10 indicates the agreement between the observed and predicted redshift distributions, a good agreement corresponding to $\langle N_z/N_{z_{\text{max}}} \rangle = 0.5$ (Section 4.3). Error bars are indicated for the confidence level of 90%.

Model	Number of GRBs in the energy range (E_{iso} in erg)					Best fit PL index	Cutoff 10^{54} erg	χ^2 (dof)	$\langle N_z/N_{z_{\text{max}}} \rangle$
	$10^{53-53.5}$	$10^{53.5-54}$	$10^{54-54.5}$	$10^{54.5-55}$	10^{55-56}				
<i>Fermi</i>/GBM, observed	12.0	14.0	5.0	3.0	0.0				
Model: PL, no evolution	15.5	8.9	4.9	2.6	2.1	-1.55±0.20	N/A	5.88	0.45±0.066
<i>Fermi</i> /GBM mean weights	1.1	1.0	1.0	1.0	1.0	-1.55±0.19		(3)	
Model: PL & density evol.	15.1	9.1	5.1	2.6	2.1	-1.57±0.21	N/A	5.41	0.35±0.066
<i>Fermi</i> /GBM mean weights	1.3	1.1	1.0	1.0	1.0	-1.57±0.18		(3)	
Model: PL & luminosity evol.	15.3	9.2	5.1	2.5	1.9	-1.61±0.23	N/A	5.11	0.31±0.066
<i>Fermi</i> /GBM mean weights	1.5	1.1	1.0	1.0	1.0	-1.59±0.18		(3)	
Model: CPL & no evolution	12.8	11.3	7.5	2.3	0.1	-1.07	3.3	1.82	0.45±0.066
<i>Fermi</i> /GBM mean weights	1.1	1.0	1.0	1.0	1.0			(2)	
Model: CPL & density evol.	12.7	11.4	7.5	2.3	0.1	-1.13	3.5	1.81	0.35±0.066
<i>Fermi</i> /GBM mean weights	1.3	1.1	1.0	1.0	1.0			(2)	
Model: CPL & luminosity evol.	12.7	11.4	7.4	2.3	0.2	-1.11	1.2	1.82	0.33±0.066
<i>Fermi</i> /GBM mean weights	1.5	1.2	1.0	1.0	1.0			(2)	
<i>Konus-Wind</i>, observed	20.0	23.0	12.0	4.0	0.0				
Model: PL, no evolution	25.7	15.3	8.7	5.2	4.1	-1.63±0.15	N/A	10.69	0.48±0.056
<i>Konus-Wind</i> mean weights	2.0	1.6	1.4	1.1	1.0	-1.57±0.12		(3)	
Model: PL & density evol.	26.0	15.2	8.5	5.3	3.9	-1.73±0.16	N/A	11.02	0.40±0.056
<i>Konus-Wind</i> mean weights	3.1	2.3	1.7	1.2	1.0	-1.61±0.10		(3)	
Model: PL & luminosity evol.	25.6	15.0	8.5	5.6	4.3	-1.79±0.17	N/A	11.76	0.35±0.056
<i>Konus-Wind</i> mean weights	5.0	3.4	2.4	1.4	1.0	-1.65±0.09		(3)	
Model: CPL & no evolution	21.0	20.8	13.7	3.4	0.1	-1.03±0.3	$2.2_{-1.0}^{+4}$	0.63	0.48±0.056
<i>Konus-Wind</i> mean weights	2.0	1.6	1.4	1.1	1.0			(2)	
Model: CPL & density evol.	20.6	20.9	13.8	3.6	0.1	-1.09±0.4	$2.1_{-1.0}^{+4}$	0.59	0.40±0.056
<i>Konus-Wind</i> mean weights	3.0	2.3	1.7	1.2	1.0			(2)	
Model: CPL & luminosity evol.	20.3	21.8	13.3	3.5	0.1	$-0.87_{-0.55}^{+0.7}$	$0.6_{-0.3}^{+1.2}$	0.39	0.37±0.056
<i>Konus-Wind</i> mean weights	5.1	3.6	2.6	1.5	1.0			(2)	

^aWe give no error on the best fit parameters for Fermi CPL models since they are not well constrained due to a degeneracy between the slope of the power law and the cutoff energy for small numbers of GRBs.

4.1. Very energetic GRBs

We start this section with a brief discussion of the main properties of very energetic GRBs (hereafter called "energetic GRBs" for simplicity), that we arbitrarily define as GRBs with $E_{\text{iso}} > 2.3 \times 10^{54}$ erg. This cut selects the six most energetic events of each instrument. Four energetic GRBs have been detected in common by *Fermi*/GBM and *Konus-Wind*: GRB 080916C, GRB 090323, GRB 120624B, and GRB 160625B. Two have been detected only by *Fermi*/GBM: GRB 090902B and GRB 140206A, and two only by *Konus-Wind*: GRB 130505A and GRB 130907A. These energetic GRBs are bright events which are detectable out to $z \geq 5$ with *Fermi*/GBM, and out to distances ranging from $z=2.07$ (GRB 130907A) to $z \geq 5$ (GRB 080916C) with *Konus-Wind*.

Figure 5 compare the properties of these eight energetic GRBs (located above the dashed line) with other GRBs in our sample. Energetic GRBs appear longer than average, with larger fluence and larger intrinsic E_{peak} . Their intrinsic durations range from 6.4 s to 189 s, with a median of 34 s, larger than the median intrinsic duration of 11.9 s for *Fermi*/GBM GRBs and of 9.1 s for *Konus-Wind* GRBs. Their observed fluences range from 6×10^{-5} erg cm^{-2} to 90×10^{-5} erg cm^{-2} , with a median of 21×10^{-5} erg cm^{-2} , larger than the median fluence of 1.6×10^{-5} erg cm^{-2} for *Fermi*/GBM GRBs in our sample and of 5.4×10^{-5} erg cm^{-2} for *Konus-Wind* GRBs in our sample. Their intrinsic E_{peak} range from 870 to 3580 keV with a median of 1850 keV, well above the median intrinsic peak energy of *Fermi* GRBs (670 keV) and *Konus-Wind* GRBs (730 keV). This last feature agrees with a known property of GRBs, namely that GRBs with large E_{iso} cannot have low intrinsic E_{peak} (Amati et al. 2009; Heussaff et al. 2013). We point out that these energetic GRBs are not specially distant sources, since their redshifts range from $z=1.24$ to $z=4.35$, with a median value $z=2.2$, close to the median of our sample. Finally, we note that the six energetic GRBs detected by *Fermi*/GBM have also been detected by the LAT, according to the *Fermi* LAT online GRB catalog⁴, indicating that GeV emission is systematically detected in energetic GRBs (see also Veres et al. 2015 about GRB 130907A). This means that the values of E_{iso} given in table 2 must be taken as lower limits because part of the energy is radiated above 100 MeV, in the energy range of the LAT. However, this very high energy emission does not change our conclusion about a cutoff energy, as explained in the next section.

Overall, we have no indication that energetic GRBs constitute a special class of events, it rather seems that they represent the high energy end of the E_{iso} distribution of long GRBs (Figure 5). This is at odds with the conclusions of Cenko et al. (2011) who claim the existence of a class of hyper-energetic GRBs, containing GRB 090323, GRB 090902B and GRB 090926A included in our sample.

4.2. Origin of the energy cutoff

The existence of a sharp structure in the distribution of E_{iso} remains puzzling for jetted GRBs since E_{iso} depends on several parameters, like the size of the energy reservoir feeding the jet E_j , the radiative efficiency of the jet η_j , and the beaming factor of the jet ($f_b = 4\pi/\Omega_j$, where Ω_j is the solid angle of the jet) according to the formula:

$$E_{\text{iso}} = E_j \times f_b \times \eta_j \quad (7)$$

A simple explanation to the observed cutoff in the distribution of the isotropic energy could be obtained if it could be attributed to a dominant term in equation 7:

1. If GRB jets have similar geometries and radiative efficiencies, or if at least the product $f_b \times \eta_j$ is similar, then the observed cutoff would mark an upper limit on E_j , the energy budget of the jet, i.e. an important constraint on the physics of the central engine and the relativistic ejection. While the estimate of E_j is very uncertain, we note that for typical values of f_b (≈ 500) and η_j (≈ 0.25), the cutoff corresponds to $E_j \approx 2 \times 10^{51}$ erg, comparable to the maximum rotational energy of magnetars (Bernardini 2015, and reference therein). The E_{iso} cutoff observed here could thus find a natural explanation within the context of magnetar models of GRBs. Nevertheless, this possibility puts stringent constraints on the efficiency of jet production in magnetars, since it requires that the rotational energy is almost entirely transferred to the jet.
2. Alternatively, if the central engine of GRBs is injecting a universal energy per unit solid angle in the jet, i.e. if $E_j \times f_b$ is similar in all GRBs, then the observed cutoff would indicate a maximum radiative efficiency, leading to an important constraint on the dissipation mechanisms and radiative processes responsible for the GRB prompt emission.

⁴ http://fermi.gsfc.nasa.gov/ssc/observations/types/grbs/lat_grbs/

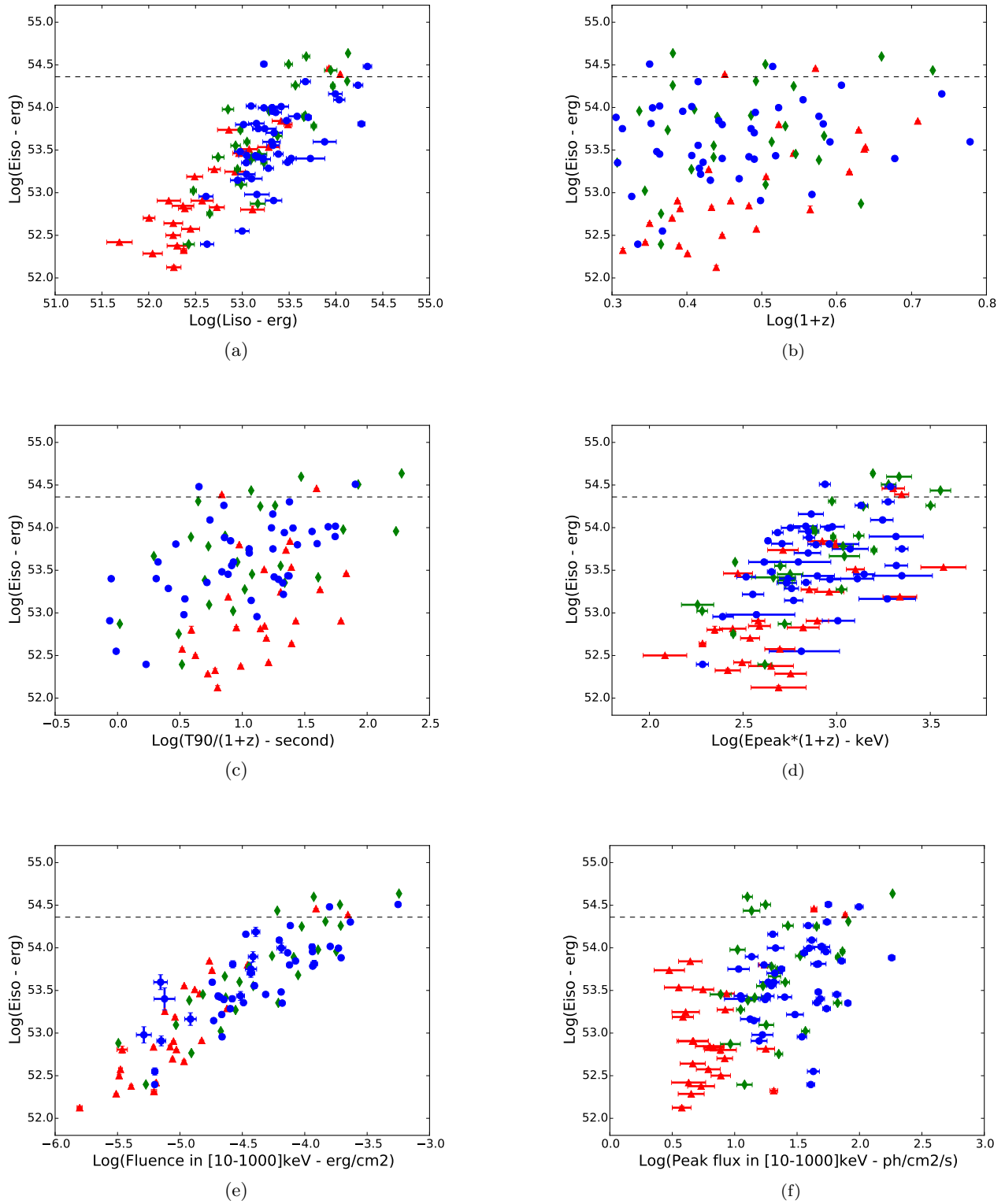


Figure 5. Distribution of E_{iso} for 95 GRBs as a function of L_{iso} (panel a), the redshift (panel b), T_{90} in the restframe (panel c), E_{pi} in the restframe (panel d), the 10 keV - 1 MeV fluence (panel e), and the peak flux (panel f). We use red triangles for *Fermi*-only GRBs, blue circles for *Konus*-only GRBs, and green diamonds for GRBs detected by *Fermi* and *Konus*. For those GRBs, we plot the values from the *Fermi*-GBM catalog. Energetic GRBs discussed in Section 4.1 are located above the dashed line.

3. Finally, if the true radiated energy $E_j \times \eta_j$ is similar in all GRBs, as suggested by Ghirlanda et al. (2013), the observed cutoff would be due to a minimum beaming angle of the jet, leading again to a new constraint on the relativistic ejection mechanism.

Unfortunately, there are no observational evidence for such simple scenarios. While we have some indications in favor of a high radiative efficiency of energetic GRBs, with η_j in the range [0.2-0.6] (Racusin et al. 2011), the situation is more complex with the beaming factor. McBreen et al. (2010) find a large dispersion of beaming factors, from $f_b \leq 180$ ($\theta_j \geq 6^\circ$) for GRB 080916C and GRB 090902B to $f_b \sim 1500$ ($\theta_j \leq 2.1^\circ$) for GRB 090323. Cenko et al. (2011), on the other hand, find less dispersed values for the same GRBs: $f_b \sim [390 - 540]$ ($\theta_j = 3.9 \pm 0.2^\circ$) for GRB 090902B to $f_b \sim [640 - 900]$ ($\theta_j = 2.8^\circ \pm_{-0.1}^{0.4}$) for GRB 090323. Regarding GRB 130907A, Veres et al. (2015) reach contrasted conclusions: the afterglow can be modeled with a single jet with a beaming factor $f_b \sim 45$ ($\theta_j \geq 12^\circ$) or with a double jet, with the internal (more energetic) jet having a large beaming factor $f_b \sim 1600$ ($\theta_j \sim 2^\circ$). Other studies of luminous GRBs with good multi-wavelength follow-up have led to beaming angles of $f_b \sim [700 - 1600]$ ($\theta_j \sim 2 - 3^\circ$) for bright GRBs (e.g. Frail et al. 2001; Grupe et al. 2006), and the most luminous GRB to date, GRB 110918A have also been suggested to be highly collimated event with $\theta_j = 1.7 - 3.4^\circ$, corresponding to a large beaming factor $f_b \approx 600 - 2200$ (Frederiks et al. 2013). Finally, detailed studies of well observed *Swift* GRBs suggest that most of them are observed off-axis, a fact that may impact these estimates (Ryan et al. 2015; Zhang et al. 2015), it is not clear however if this is also the case for the very bright GRBs discussed here. We conclude that the data at hand are not sufficient to firmly settle the issue of the "homogeneity" of the jets of energetic GRBs. Overall, it is surprising to realize that such bright GRBs do not benefit from follow-up observations that permit measuring their beaming factors without ambiguity.

Another source of uncertainty arises if a significant fraction of the energy escapes in another electromagnetic channel, for instance in high energy gamma-rays (several GeV). We note that the most luminous GRBs in our sample are all detected with *Fermi*/LAT, showing that their emission is not limited to the energy range of the *Fermi*/GBM, and their bolometric energy would increase if we consider the flux measured with the LAT. Suppressing the observed energy cutoff would nevertheless require that these GRBs radiate most of their energy above several tens of MeV. This is in contradiction with the analysis of the energetics of some of the most luminous long GRBs performed by Ackermann et al. (2013), which shows that keV–MeV photons dominate the energetics, with 10% or less of the total energy being radiated above 100 MeV.

In view of these various sources of error it appears quite difficult to state if the cutoff observed on E_{iso} is due to a cutoff on the jet energy E_j or to some radiative or beaming effect. Measuring E_j directly through the radiocalorimetry (Frail et al. 2000) of some very energetic GRBs might offer a way to settle this issue.

In conclusion, since $E_{\text{iso}}/4\pi$ represents the electromagnetic energy radiated per unit of solid angle, the observation of a cutoff E_{iso} suggests the existence of a *maximum energy radiated per unit of solid angle*. While the very energetic GRBs discussed here radiate considerable energy, they are not necessarily those with the largest energy reservoirs. Indeed, GRBs with larger energy reservoirs and smaller E_{iso} could exist, if they have a different radiative pattern (broader jets) or a smaller radiative efficiency.

4.3. A detour through the GRB formation rate

In this section, we complete our analysis with a comparison of the observed and predicted redshift distributions for the six GRB world models under study. For each observed GRB we compute two numbers: $N(<z_i)$, the number of such GRBs that are closer than the redshift of the burst, and $N(<z_{\text{max}})$, the number of such GRBs within the horizon z_{max} . These two numbers depend on the choice of a GRB world model. Considering that the observed GRBs are randomly chosen among the observable GRBs, if the world model is correct the ratio $N(<z_i)/N(<z_{\text{max}})$ is randomly distributed in [0,1] with a mean =0.5. The distribution of $N(<z_i)/N(<z_{\text{max}})$ can thus be used to test GRB world models: a mean close to 0.5 indicates a GRB world model that is acceptable, while a mean incompatible with 0.5 indicates a GRB world model which must be rejected because it predicts a redshift distribution incompatible with the observed redshift distribution.

Column 10 of Table 4 shows that similar results are obtained with *Fermi*/GBM and *Konus-Wind*, suggesting that models with no evolution are favored by the data. This is however a low significance effect, and further studies are required to assess the compatibility of specific GRB world models with the observed $N(<z_i)/N(<z_{\text{max}})$ distribution. ⁵

⁵ In the earlier version of this paper, the observed contradiction between the results obtained by *Fermi* and *Konus* was due to the error on the calculation of *Konus* GRB horizon.

4.4. Are energetic GRBs standard candles?

If it is confirmed, the existence of a limit on the GRB isotropic energy would permit using energetic GRBs as standard candles visible out to large redshifts. We briefly discuss here the expected number of such GRBs, using the statistics of *Fermi* detections. Figure 5 shows that the six energetic GRBs detected by *Fermi* have peak fluxes larger than $10 \text{ ph cm}^{-2} \text{ s}^{-1}$ in the energy range 10-1000 keV. We thus consider only those GRBs in the following discussion based on the Third Fermi GBM GRB Catalog (Narayana Bhat et al. 2016). This catalog contains 247 GRBs with a peak flux larger than $10 \text{ ph cm}^{-2} \text{ s}^{-1}$ in the energy range 10-1000 keV. 40 of them have a redshift, 11 with $z < 1$ and 29 with $1 \leq z \leq 5$. Among them 5 are energetic GRBs with $E_{\text{iso}} > 2.3 \times 10^{54} \text{ erg}$ (we exclude GRB 160625B which is outside the six year period covered by the Third Fermi GBM GRB Catalog). Assuming that the fraction of energetic GRBs is the same for bright GRBs with and without a redshift, we expect $5 \times (247/40) = 31$ energetic GRBs in six years, corresponding to a rate of $\approx 5/\text{yr}$. These GRBs may represent an interesting tool to explore the Hubble diagram at large redshifts ($z \geq 1.5$) if the E_{iso} cutoff discussed here does not evolve with the redshift.

5. CONCLUSION

The main conclusion of this paper is the existence of a sharp cutoff of the E_{iso} distribution of *Konus-Wind* and *Fermi*/GBM GRBs around $1 - 3 \times 10^{54} \text{ erg}$. Given the scarcity of such energetic GRBs, this cutoff can only be observed by instruments with a large effective sky coverage (in yr steradian). This is obviously the case of *Konus-Wind* launched 22 years ago, and to a lesser extent the case of *Fermi* launched 8 years ago, both instruments monitoring nearly the whole sky (except 30% occulted by the Earth for *Fermi*/GBM).

We have shown that this cutoff is an intrinsic GRB property, which must be taken into account by GRB world models, which may otherwise consider a slope of the bright end of the GRB energy function which is too steep. After discussing diverse possibilities for the origin of this feature, we conclude that it is necessary to measure the fundamental properties of the jet, like the beaming angle or the true energy budget, more accurately before we can decide if this cutoff is due to the progenitor or to the physical processes at work in the jet.

DT gratefully acknowledge financial support from the OCEVU LabEx, France. YZ welcomes financial support from IRAP (UMR5277/CNRS/UPS). DDF gratefully acknowledges support from RFBR grants 15-02-00532-i and 16-29-13009-ofi-m. The authors thank the referee whose comments contributed to improve the content and clarity of the manuscript. This article made use of the GRB table maintained by J. Greiner, available at <http://www.mpe.mpg.de/~jcg/grbgen.html>.

Facilities: *Fermi*, *Swift*, *WIND*

Software: Python

REFERENCES

- Ackermann, M., Ajello, M., Asano, K., et al. 2013, *ApJS*, 209, 11
 Ackermann, M., Ajello, M., Asano, K., et al. 2014, *Science*, 343, 42
 Amati, L., Frontera, F., & Guidorzi, C. 2009, *A&A*, 508, 173
 Aptekar, R. L., Frederiks, D. D., Golenetskii, S. V., et al. 1995, *SSRv*, 71, 265
 Band, D., Matteson, J., Ford, L., et al. 1993, *ApJ*, 413, 281
 Bernardini, M. G. 2015, *Journal of High Energy Astrophysics*, 7, 64
 Bloom, J. S., Frail, D. A., & Sari, R. 2001, *AJ*, 121, 2879
 Butler, N. R., Bloom, J. S., & Poznanski, D. 2010, *ApJ*, 711, 495
 Cenko, S. B., Frail, D. A., Harrison, F. A., et al. 2011, *ApJ*, 732, 29
 Coward, D. M., Howell, E. J., Branchesi, M., et al. 2013, *MNRAS*, 432, 2141
 Dai, X. 2009, *ApJL*, 697, L68
 Daigne, F., Rossi, E. M., & Mochkovitch, R. 2006, *MNRAS*, 372, 1034
 Deng, C.-M., Wang, X.-G., Guo, B.-B., et al. 2016, *ApJ*, 820, 66
 Firmani, C., Avila-Reese, V., Ghisellini, G., & Tutukov, A. V. 2004, *ApJ*, 611, 1033
 Frail, D. A., Waxman, E., & Kulkarni, S. R. 2000, *ApJ*, 537, 191
 Frail, D. A., Kulkarni, S. R., Sari, R., et al. 2001, *ApJL*, 562, L55
 Frederiks, D. D., Hurley, K., Svinkin, D. S., et al. 2013, *ApJ*, 779, 151
 Gehrels, N., Ramirez-Ruiz, E., & Fox, D. B. 2009, *ARA&A*, 47, 567
 Gendre, B., Stratta, G., Atteia, J. L., et al. 2013, *ApJ*, 766, 30
 Ghirlanda, G., Ghisellini, G., Salvaterra, R., et al. 2013, *MNRAS*, 428, 1410
 Golenetskii, S., Aptekar, R., Mazets, E., et al. 2013, *GRB Coordinates Network*, 14808, 1
 Gruber, D., Goldstein, A., Weller von Ahlefeld, V., et al. 2014, *ApJS*, 211, 12
 Grupe, D., Brown, P. J., Cummings, J., et al. 2006, *ApJ*, 645, 464
 Guetta, D., Piran, T., & Waxman, E. 2005, *ApJ*, 619, 412
 Heussaff, V., Atteia, J.-L., & Zolnierowski, Y. 2013, *A&A*, 557, A100

- Hopkins, A. M. & Beacom, J. F. 2006, *ApJ*, 651, 142
- Howell, E. J., Coward, D. M., Stratta, G., Gendre, B., & Zhou, H. 2014, *MNRAS*, 444, 15
- Kocevski, D. & Liang, E. 2006, *ApJ*, 642, 371
- Levan, A. J., Tanvir, N. R., Starling, R. L. C., et al. 2014, *ApJ*, 781, 13
- Lien, A., Sakamoto, T., Gehrels, N., et al. 2014, *ApJ*, 783, 24
- Kistler, M. D., Yüksel, H., Beacom, J. F., & Stanek, K. Z. 2008, *ApJL*, 673, L119
- Li, L.-X. 2008, *MNRAS*, 388, 1487
- Maselli, A., Melandri, A., Nava, L., et al. 2014, *Science*, 343, 48
- McBreen, S., Krühler, T., Rau, A., et al. 2010, *A&A*, 516, A71
- Meegan, C., Lichti, G., Bhat, P. N., et al. 2009, *ApJ*, 702, 791
- Narayana Bhat, P., Meegan, C. A., von Kienlin, A., et al. 2016, *ApJS*, 223, 28
- Perley, D. A., Cenko, S. B., Corsi, A., et al. 2014, *ApJ*, 781, 37
- Pescalli, A., Ghirlanda, G., Salvaterra, R., et al. 2015, *ArXiv e-prints*
- Petrosian, V., Kitanidis, E., & Kocevski, D. 2015, *ApJ*, 806, 44
- Racusin, J. L., Oates, S. R., Schady, P., et al. 2011, *ApJ*, 738, 138
- Ryan, G., van Eerten, H., MacFadyen, A., & Zhang, B.-B. 2015, *ApJ*, 799, 3
- Salvaterra, R. & Chincarini, G. 2007, *ApJL*, 656, L49
- Salvaterra, R., Guidorzi, C., Campana, S., Chincarini, G., & Tagliaferri, G. 2009, *MNRAS*, 396, 299
- Salvaterra, R., Campana, S., Vergani, S. D., et al. 2012, *ApJ*, 749, 68
- Shahmoradi, A. 2013, *ApJ*, 766, 111
- Tan, W.-W. & Wang, F. Y. 2015, *MNRAS*, 454, 1785
- Tsvetkova, A., Frederiks, D., Golenetskii, S., et al. 2017, *arXiv:1710.08746*
- Turpin, D., Heussaff, V., Dezalay, J.-P., et al. 2016, *ApJ*, 831, 28
- Veres, P., Corsi, A., Frail, D. A., Cenko, S. B., & Perley, D. A. 2015, *ApJ*, 810, 31
- Vestrand, W. T., Wren, J. A., Panaitescu, A., et al. 2014, *Science*, 343, 38
- von Kienlin, A., Meegan, C. A., Paciasas, W. S., et al. 2014, *ApJS*, 211, 13
- Wanderman, D. & Piran, T. 2010, *MNRAS*, 406, 1944
- Zhang, B.-B., van Eerten, H., Burrows, D. N., et al. 2015, *ApJ*, 806, 15
- Zitouni, H., Daigne, F., Mochkovich, R., & Zerguini, T. H. 2008, *MNRAS*, 386, 1597